



Contents lists available at ScienceDirect

International Journal of Biological Macromolecules

journal homepage: www.elsevier.com/locate/ijbiomac

Tailoring the mechanical and rheological properties of poly(lactic acid) by sterilizing UV-C irradiation

Ábris Dávid Virág^a, Csenge Tóth^{a,b}, Péter Polyák^{c,d}, Marta Musioł^e, Kolos Molnár^{a,f,*}^a Department of Polymer Engineering, Faculty of Mechanical Engineering, Budapest University of Technology and Economics, Műegyetem rkp. 3. H-1111 Budapest, Hungary^b MTA-BME Lendület Lightweight Polymer Composites Research Group, Műegyetem rkp. 3. H-1111 Budapest, Hungary^c Department of Food, Agricultural and Biological Engineering, College of Food, Agricultural, and Environmental Sciences, The Ohio State University, 1680 Madison Avenue, 44691 Wooster, OH, USA^d Laboratory of Plastics and Rubber Technology, Department of Physical Chemistry and Materials Science, Faculty of Chemical Technology and Biotechnology, Budapest University of Technology and Economics, Műegyetem rkp. 3. H-1111 Budapest, Hungary^e Centre of Polymer and Carbon Materials, Polish Academy of Sciences, 34, M. Curie-Skłodowska St, 41-819 Zabrze, Poland^f HUN-REN-BME Research Group for Composite Science and Technology, Műegyetem rkp. 3. H-1111 Budapest, Hungary

ARTICLE INFO

Keywords:
Crystallinity
PLA
Molecular changes
Cross-WLF
Raman spectroscopy

ABSTRACT

In this study, we irradiated amorphous (A) and semi-crystalline (SC) poly(lactic acid) (PLA) with different UV-C doses up to 2214 kJ/m². We achieved an average crystallinity of 43 % by heat treatment, which was unaffected by UV-C irradiation. Modulated differential scanning calorimetry showed that crystal polymorphs and the ratio of rigid amorphous and mobile amorphous phases were also unaffected. Using gel permeation chromatography analysis, we showed that the degradation mechanism was noncatalytic random scission, and the initial molar mass was reduced by >90 % at a dose of 2214 kJ/m² for both A- and SC-PLA samples. Our Raman spectroscopy results indicated that the probability of the formation of oxygen-containing groups increases with increasing UV-C doses. Since we found that the mechanical properties of PLA films can be tailored with UV-C light, we proposed a method to predict the overall tensile curve as a function of the UV-C dose. We also proposed a modified Cross-WLF model to describe the effect of UV-C irradiation on viscosity up to 55 % molar mass reduction. The models allow us to estimate the limits of recyclability and reusability of sterilised PLA products.

1. Introduction

Medical devices are classified into three categories based on their risk level (Class I, II and III, from low to high risk). The class determines the level of regulation and control needed to ensure the safety and effectiveness of the device [1]. Due to their moderate price and their versatility, plastics are widely used in all categories, from single-use packaging (transparent films) to medical implants (orthopaedic implants, stents). Therefore, it is very important to know the short- and long-term effects of various sterilisation processes on plastics. The most common sterilisation agents are ethylene oxide (EtO), ozone (O₃) and hydrogen peroxide (H₂O₂), but heat treatment (steam or dry heat), and radiation are also widely used [2]. Products with inherent antibacterial properties are also common, but often still require a sterilisation step

before use [3].

To achieve sustainable economy, bioplastics are preferred as materials of medical devices [4]. Polylactic acid (PLA) is a biocompatible, bioresorbable, and biodegradable polymer that can be processed with a variety of manufacturing methods [5,6]. Therefore, PLA-based products are widely used in medical applications [7]. Transparent PLA films are used as medical packaging [8]; 3D-printed PLA and PLA composite scaffolds are used in bone tissue engineering [9]; PLA fibres are utilised as absorbable surgical sutures [10]; and electrospun PLA nanofibers are applied as drug delivery systems [11]. All these applications require sterile products. However, sterilisation can cause adverse changes in the properties of PLA. For example, its surface and optical quality and also its mechanical properties may deteriorate [12,13].

Ivanova et al. [14] found that steam sterilisation increases the

* Corresponding author at: Department of Polymer Engineering, Faculty of Mechanical Engineering, Budapest University of Technology and Economics, Műegyetem rkp. 3, H-1111 Budapest, Hungary.

E-mail addresses: viraga@pt.bme.hu (Á.D. Virág), tothcs@pt.bme.hu (C. Tóth), polyak.10@osu.edu (P. Polyák), mmusiol@cmpw-pan.pl (M. Musioł), molnar@pt.bme.hu (K. Molnár).

<https://doi.org/10.1016/j.ijbiomac.2024.134247>

Received 28 March 2024; Received in revised form 23 July 2024; Accepted 27 July 2024

0141-8130/© 2024 The Authors. Published by Elsevier B.V. This is an open access article under the CC BY license (<http://creativecommons.org/licenses/by/4.0/>).

surface roughness and the wettability of PLA films, which promotes the proliferation of cells. However, changes in mechanical properties were not investigated. Savaris et al. [15] investigated the effect of five different sterilisation methods (EtO, saturated steam, H₂O₂ plasma, electron beam irradiation, gamma irradiation) on the morphological, physical, chemical and thermal properties of PLA films. The authors found that of the processes tested, saturated steam (121 °C at a pressure of 2 bar for 20 min) caused the most significant structural changes due to the high pressure and temperature. Therefore, saturated steam is not recommended for the sterilisation of PLA products. Garnica-Bohórquez et al. [16] subjected 3D-printed PLA samples to a sterilisation protocol used in a public hospital in Colombia, which involved formaldehyde steam (65 °C for 20 h) sterilisation. The authors examined the mechanical behaviour of the PLA and found that its tensile properties deteriorated due to the sterilisation procedure. Krug et al. [17] studied the effect of ethylene oxide and gamma irradiation on injection-moulded PLA samples. EtO sterilisation caused a slight decrease in viscosity and elongation at break, while gamma irradiation resulted in degradation. Overall, the European Commission and the Environmental Protection Agency (United States) identified EtO as a substance of concern due to its carcinogenic and mutagenic effects, so its use in sterilisation is expected to decline [18,19].

Mansouri et al. [20] examined the radiation-induced degradation mechanisms of PLA films. At low doses, electron beam irradiation causes random chain scission. Consequently, the decrease in molar mass decreases the transition temperatures and deteriorates mechanical properties. Benyathiar et al. [21] subjected PLA films to gamma and electron beam irradiation and found that both caused degradation. Molar mass loss causes deterioration of thermal and mechanical properties. Therefore, it must be considered if the sterilised product is subjected to mechanical loads.

UV-C sterilisation has become widespread in recent years, in the context of the SARS-CoV-2 epidemic. Therefore, its effects on polymers are less explored. Only a few studies have addressed the loss of mechanical properties of PLA after exposure to UV-C irradiation [22,23]. However, the structure–property relationship between degradation and material properties has not been investigated so far. Besides sterilisation, UV-C radiation also has potential applications in plastic waste treatment. Brown et al. [24] showed that the reduced molar mass caused by UV irradiation helps the enzymatic hydrolysis of PLA. Therefore, it increases the rate of biodegradation. In a previous study [25], we investigated the changes in molar mass and the mechanical and rheological properties of UV-C irradiated amorphous PLA films. We found that increasing irradiation time leads to a ductile–brittle transition in tensile properties. The amorphous PLA films can withstand 13 sterilisation cycles without significant changes in tensile strength and modulus.

The present study aims to investigate the changes in the molecular structure of PLA due to UV-C irradiation. We study the effect of crystallinity on various mechanical, thermal and rheological properties. We set up models to predict various material properties as a function of the irradiation dose. These can be used to estimate the properties of the product as a function of the number of sterilisation cycles, thus

guaranteeing the safe use of medical devices in the long term.

2. Materials and methods

2.1. Material and sample preparation

The entire sample preparation process is shown in Fig. 1. We used an extrusion-grade polylactic acid (PLA), Ingeo 4032D, supplied by NatureWorks LLC (Plymouth, MN, USA). The bulk density of this PLA is 1.24 g/cm³ and its D-lactide content is 1.4–2 % only [26]. We dried the PLA in a Faithful WGLL-125 BE (Faithful Instrument (Hebei) Co., Ltd., Huanghua, China) hot air oven at 80 °C for 4 h before processing. We produced optically transparent PLA films with a thickness of 165 ± 15 µm using a Labtech Scientific 25-30C single-screw extruder (Labtech Engineering, Thailand) and an LCR300 flat film line (Labtech Engineering, Samutprakarn, Thailand). The diameter and the length/diameter (L/D) ratio of the general-purpose three-zone screw were 25 mm and 30, respectively. The temperature profile from the hopper to the die was 200–200–210–210 °C, and the temperature of the die was set to 220 °C. The production process is detailed more in our previous study [25].

Then, half of the samples were subjected to post-crystallisation heat treatment. The post-crystallisation heat treatment of the amorphous films was carried out as follows: we clamped the films in a wooden frame to avoid their shrinkage, then we placed them in the oven. The samples were annealed at 100 °C for 2 h for the highest possible crystalline fraction [27]. We investigated amorphous (A) and semi-crystalline (SC) PLA film samples. After the heat treatment, we placed the samples in sealed packages for one week to ensure physical ageing. We placed grains of silica gel in the packages to prevent the influence of moisture.

After that, UV-C irradiation was carried out in our custom-built degradation chamber. The chamber is equipped with two TUV30W Longlife SVL (Philips, Amsterdam, the Netherlands) mercury vapour tube lamps. The parameters of the chamber can be found in our previous study [25]. We irradiated the PLA films for 0, 0.25, 0.5, 0.75, 1, 2, 4 and 8 h in an air atmosphere at 20 °C and 41 % relative humidity. The prepared disk- and dumbbell-shape film specimens were placed directly under the tube at a distance of 5 cm, where irradiance was 76.9 W/m². Therefore, the applied doses were 0 (non-treated reference), 69, 138, 208, 277, 553, 1107 and 2214 kJ/m², respectively.

2.2. Gel permeation chromatography (GPC) analysis

We subjected the samples to GPC analysis in order to ascertain their molar mass and molar mass dispersity. The samples were prepared by dissolving them in chloroform at a concentration of 0.3 % w/v and passed through the solvent delivery system Nexera HPLC/UHPLC Pump - LC-40D XR (Shimadzu, Kyoto, Japan), at 35 °C with a flow rate of 1 mL/min. This process involved using two Mixed C Styragel (Agilent Technologies, Inc., Santa Clara, CA, United States) columns with a mixed bed ($M_w = 200\text{--}2,000,000$) for analysis and a refractive index detector (Shodex SE 61, Showa Denko, Munich, Germany). Narrow molar-mass dispersity polystyrene standards from EasiCal® Pre-

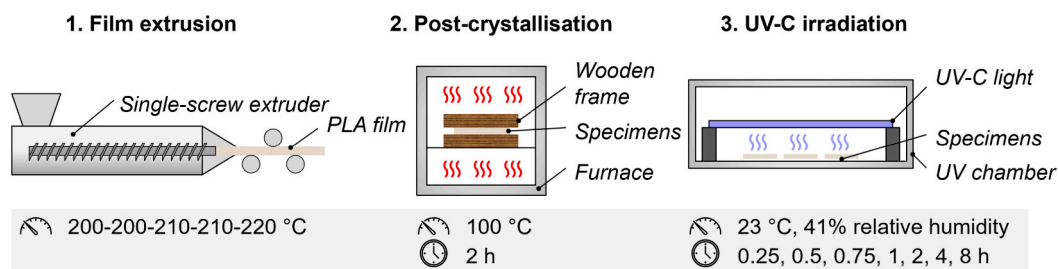


Fig. 1. Specimen preparation process.

prepared Calibration Kits provided by Agilent Technologies, Inc. is a systematic approach to creating a calibration curve for accurately determining the molar mass distribution of polymers, which was also used for this analysis.

2.3. Raman spectroscopy

Raman spectra were obtained with the use of a Thermo Fisher Scientific (Waltham, MA, USA) DXR3 Raman Imaging Microscope equipped with Olympus viewing optics. The instrument used a helium-neon laser, which emitted photons with a wavelength of 632 nm (1.96 eV). Scanning and data processing were carried out with the OMNIC Spectra Software Version 9. Spectral data was collected in the 3500–100 1/cm wavenumber region with a resolution of 1.0 1/cm. The instrument captured the entire range with a single exposure of the charge-coupled device (CCD) to avoid stitching artefacts. The samples were prepared as follows. First, the investigated A-PLA films were fastened between two rectangular pieces of metal. About half of the film was held tight between the rectangular pieces of metal, whereas the other half hung over the edge. The overhanging piece was cut off at the surface of the metal with a scalpel; the operation revealed a freshly cut cross-section of the film. This cross-section was investigated by the instrument. We displayed the results in 3D by processing the Raman data with MATLAB software written by our research team.

2.4. Modulated differential scanning calorimetry

We performed modulated differential scanning calorimetry (MDSC) in accordance with the ISO 19935-2:2020 standard using a TA Instruments Q2000 (TA Instruments, USA) differential scanning calorimeter. The weight of the samples was 8–10 mg. We applied a heat/cool/heat cycle between 0 and 200 °C with a heating/cooling rate of 5 °C/min. The amplitude of modulation was 1 °C, with a period of 60 s. The test was performed three times in a nitrogen atmosphere with a purge flow rate of 50 mL/min.

Using the TA Universal Analysis software, we determined the glass transition temperature (T_g) as the midpoint on the reversing heat flow curves of the 1st cycle. The reversing component shows heat capacity-related events such as melting and glass transition, and the non-reversing component describes kinetic events such as cold crystallisation and relaxation. The melting points (T_m) were determined as the peak maximum on the 1st reversing heat flow signal. The weight ratio of the crystalline (X_C), the mobile amorphous (X_{MAF}), and the rigid amorphous fraction (X_{RAF}) were determined by Eqs. (1)–(3), respectively.

$$X_C(\%) = \frac{\Delta H_m - \Delta H_{cc}}{\Delta H_m^0} \cdot 100, \quad (1)$$

where ΔH_m is the crystal melting enthalpy calculated as the area under the melting peak, ΔH_{cc} is the cold crystallisation enthalpy calculated as the area under the cold crystallisation peak and ΔH_m^0 is the crystal melting enthalpy of 100 % crystalline PLA. Based on the literature, the value of ΔH_m^0 ranges from 82 J/g to 203 J/g, with 106 J/g and 93 J/g being the most common ones [28]. An average X_C was calculated using $\Delta H_{m1}^0=106$ J/g and $\Delta H_{m2}^0=93$ J/g.

$$X_{MAF}(\%) = \frac{\Delta C_p}{\Delta C_p^0} \cdot 100, \quad (2)$$

where ΔC_p is the measured heat capacity step at T_g and $\Delta C_p^0=0.45$ J/(g·°C) is the heat capacity step at T_g of the 100 % amorphous PLA determined from the neat A-PLA samples.

$$X_{RAF}(\%) = 1 - X_C - X_{MAF}, \quad (3)$$

The ratio of α' and α crystals was determined by the deconvolution of the time-dependent reversing heat flow signal ($RHF_{measured}(t)$) using the

Peak Deconvolution module in OriginPro 2024 software (Fig. 2). First, the baseline was approximated with a straight line (Eq. 4).

$$f_{base}(t) = A_f \cdot t + B_f \quad (4)$$

where A_f (slope) and B_f (intercept) are fitted parameters.

The double melting peak was then divided into two separate peaks, each of which can be described with a Gaussian distribution function (Eq. 5). The melting enthalpy of the crystals is given by the A_g parameter.

$$g_x(t) = \frac{A_g \cdot e^{-\frac{4 \cdot \ln(2) \cdot (t-B_g)^2}{C_g^2}}}{C_g \cdot \sqrt{\frac{\pi}{4 \cdot \ln(2)}}} \quad (5)$$

where X denotes the type of crystal (α' and α), A_g is the area under the curve, B_g is the peak value and C_g is the width at half maximum. The resulting reversing heat flow model curve ($RHF_{model}(t)$) can be calculated as the sum of these curves (Eq. 6):

$$RHF_{model}(t) = f_{base}(t) + g_{\alpha'}(t) + g_{\alpha}(t) \quad (6)$$

2.5. Tensile testing

To determine the effect of irradiation on mechanical properties, we carried out tensile tests on dumbbell specimens. The specimens were cut from the extruded films with a manual punching machine. Cutting direction was parallel to the extrusion direction. The shape was in accordance with the type 5 A dumbbell specimen of the ISO 527-2:2012 standard, with a total length of 75 mm. We carried out uniaxial tensile tests in accordance with the same standard, with a Z005 (Zwick GmbH, Ulm, Germany) universal tensile tester equipped with 200 N-rated Zwick 8131 screw grips. 9 displacement-controlled tests were performed in every case at 25 °C. Gripping distance was 50 mm, and crosshead speed was 2 mm/min. Samples irradiated for 4 and 8 h could not be tested because they degraded to the extent that they broke during gripping. The force was measured with a high-precision Zwick 5 kN load cell with a resolution of 0.01 N. We calculated strain as the ratio of crosshead displacement and gripping distance. The tensile modulus was determined as the slope of a chord between 0.05 % and 0.15 % strains. 0.15 % strain was used instead of 0.25 % strain specified in the standard because the elongation at break of highly degraded samples was <0.25 %.

2.6. Dynamic mechanical analysis

To investigate the dynamic mechanical behaviour of the undegraded and degraded films, we carried out temperature sweeps with a Q800 (TA instruments, New Castle, DE, USA) dynamic mechanical analyser (DMA) using a film tension clamp. Measurements were performed on 6 mm-wide, 35 mm-long samples at 1 Hz, using a 3 °C/min heating rate, from

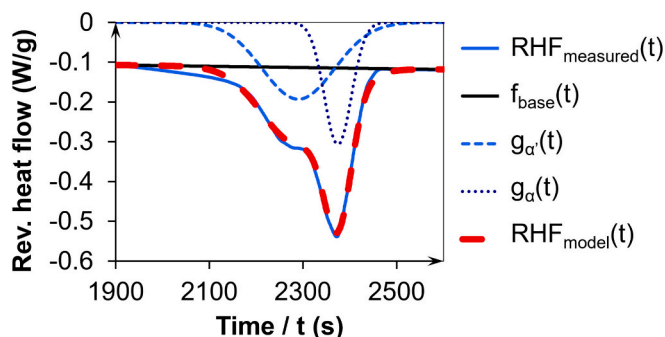


Fig. 2. Deconvolution of the reversing heat flow curve.

25 to 170 °C. We used an amplitude of 5 μm , which was within the linear viscoelastic region, verified by amplitude sweeps.

2.7. Rheological characterisation

To investigate melt flow properties, we used an MCR-301 (Anton-Paar, Graz, Austria) oscillatory shear rheometer with a parallel plate setup (plate diameter = 25 mm, gap size = 1 mm). For each test, we used 6 discs of 25 mm diameter cut from the extruded films. Frequency sweeps were then carried out at 180 °C between 0.0628 and 628 rad/s. Before the tests, a five-minute soak time was used to achieve thermal equilibrium and allow relaxation processes. The 5 % strain amplitude was chosen to be within the linear viscoelastic region.

3. Results and discussion

3.1. Molecular changes due to UV-C irradiance

3.1.1. Changes in molar mass (GPC results)

We performed GPC to analyse the effects of UV-C irradiation on molar mass and structure. The molar mass distribution of neat PLA is monomodal, and with increasing UV-C dose (d), this distribution shifts towards lower molar mass values in both amorphous (A-PLA) and semi-crystalline (SC-PLA) PLA (Fig. 3/a, b). The changes in the number (M_n) and weight average molar mass (M_w) for the A-PLA and the SC-PLA are shown in Fig. 3/c.

The initial M_w of the SC-PLA samples was 5 % lower than that of the A-PLA samples, which can be due to the heat treatment [29]. The highest applied UV-C dose (2214 kJ/m^2) reduced the initial molar mass by >90 %. The M_n of the A-PLA and the SC-PLA decreased from 107.2 kg/mol to 6.3 kg/mol and from 109.4 kg/mol to 7.9 kg/mol, respectively. Similarly, the weight averages decreased from 208.0 kg/mol to 15.8 kg/mol and from 197.7 kg/mol to 19.2 kg/mol in the case of the A-

PLA and the SC-PLA, respectively.

Up to the dose of 553 kJ/m^2 (where molar mass was about 20 % of the original molar mass), dispersity (D) has not changed considerably (see Fig. 3/c). In contrast, from 553 kJ/m^2 to 2214 kJ/m^2 , there was an increase in dispersity from $D = 1.92$ to 2.5. The increase in the dispersity of both PLA samples can be attributed to two factors. First, increasing D values suggest that random chain fragmentation is the prevalent mechanism in the degradation process, which leads to the breakdown of the polymer backbone and the formation of lower molar mass species [30,31]. Second, the rate of chain scission depends on the distance from the surface and is expected to result in position-dependent average molecular weight. The correlation between the distance from the surface and the extent of degradation is discussed in Section 3.1.2.

The reciprocal of M_n is directly proportional to the UV-C dose (Fig. 3/e). This means the degradation process is non-catalytic random chain scission for both A- and SC-PLA [32]. The presence of crystalline parts did not change the rate of degradation up to 553 kJ/m^2 , but it slightly slowed the degradation process thereafter (Fig. 3/e).

Based on these results, the dependence of M_n on the UV-C dose can be described with Eq. (7):

$$M_n = \frac{1}{A_M \cdot d + B_M}, \quad (7)$$

where A_M and B_M are fitted constants and $D_{avg} = 1.92$. M_w can be approximated by Eq. (8):

$$M_w = D_{avg} \cdot M_n = \frac{D_{avg}}{A_M \cdot d + B_M}. \quad (8)$$

Fig. 3/b shows that the change in molar mass due to UV-C irradiation can be well predicted by Eqs. 4–5 ($RMSE < 4.5$).

3.1.2. Changes in chemical structure (Raman spectroscopy results)

We monitored the radiation-induced degradation with Raman

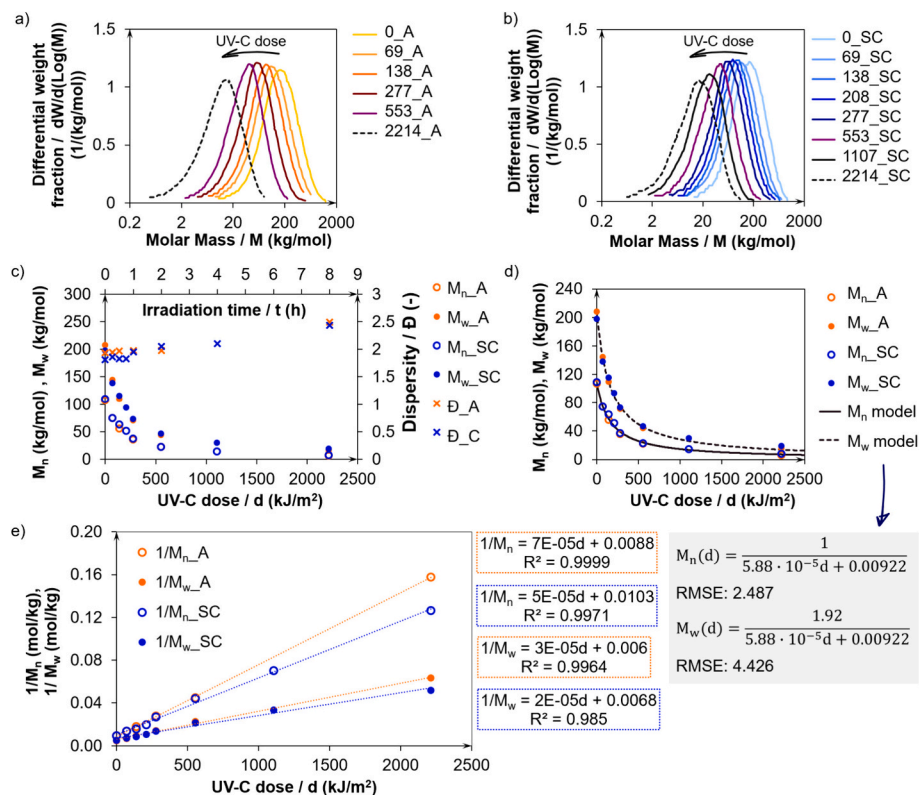


Fig. 3. Molar mass reduction due to UV-C irradiation: a), b) show the molar mass distributions of the A-PLA and SC-PLA samples; c) number- (M_n) and weight-average (M_w) molar mass as a function of UV-C dose; d) & e) fitted models.

spectroscopy. As PLA macromolecules contain multiple groups that absorb photons in the infrared wavelength range, the Raman spectrum of these polyesters is also expected to contain several absorption bands. Our results indicate that the resonances of both the aliphatic and the oxygen-containing groups can be observed well on the Raman spectrum of A-PLA (Fig. 4/a).

Since the resonances are clearly observable, and the signal-to-noise ratio is also excellent, the Raman spectrum can be a basis for the qualitative and quantitative analysis of irradiation-induced degradation. As a first step of the qualitative analysis, peaks have been assigned to individual groups (Fig. 4/a) [33,34]. We observed that UV-C irradiation affects the height of the triplet peak around 2900 $1/\text{cm}$ and concluded that the degradation mechanism involves the formation of new aliphatic

groups. Our assumption is corroborated by previously published papers [35], and our earlier studies [25].

A possible degradation mechanism that alters the amount of aliphatic end groups is demonstrated in Fig. 4/b. The degradation leads to the formation of methylene groups, which are not present in the reference sample that was not subjected to irradiation (0_A). As the degradation progresses, the number of methylene groups increases. In the case of polyhydroxyalkanoates, the absorbance peaks that belong to methyl and methylene groups were shown to appear in the same wavenumber regions [36]. Therefore, the formation of new methylene groups contributes to the increasing amplitude of the peaks attributed to the aliphatic end groups [35,36].

Even though this mechanism is supported by multiple independent

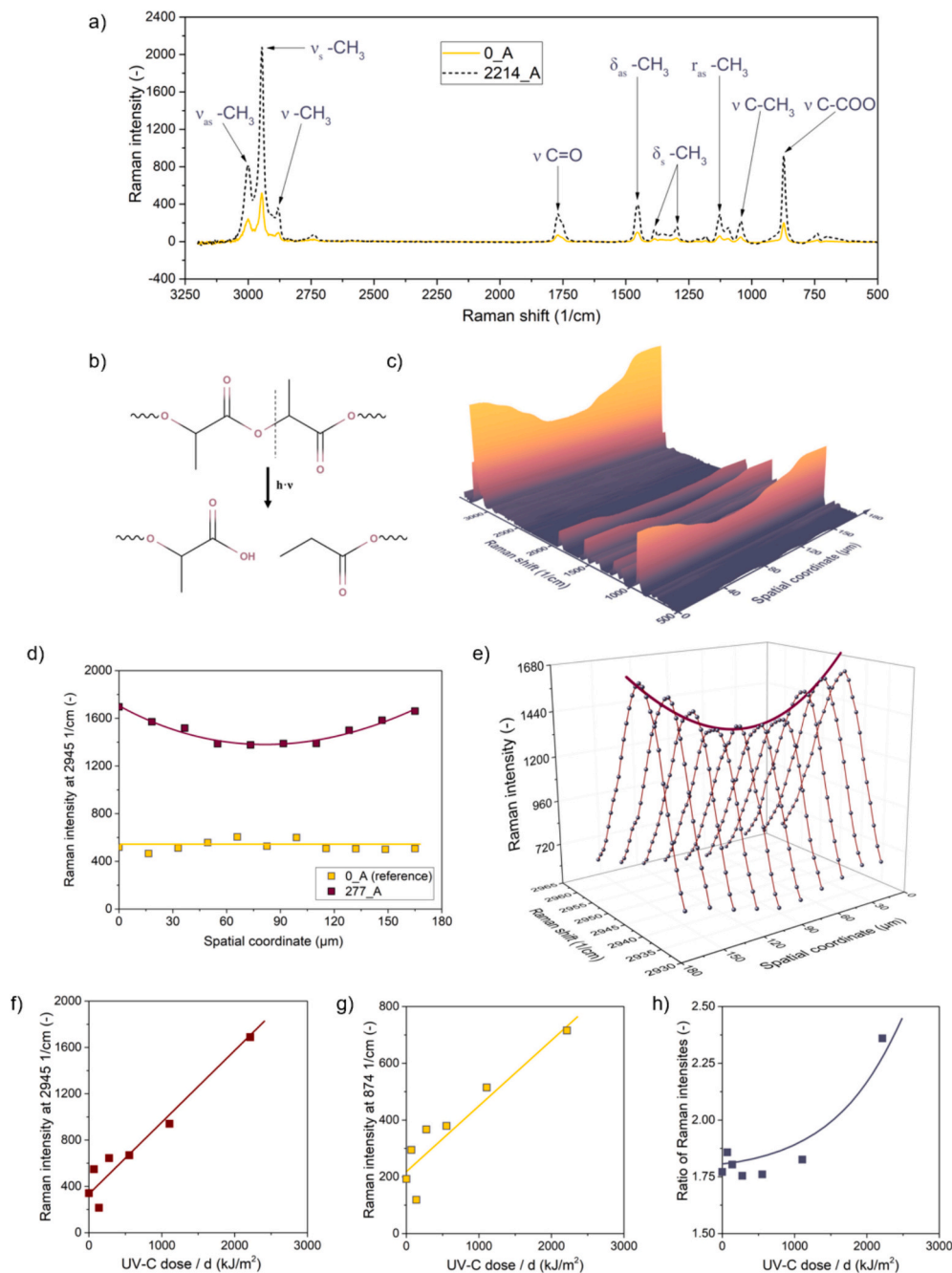


Fig. 4. Results of the Raman analysis: a) Raman spectrum of the neat and irradiated A-PLA, b) a possible UV-C degradation mechanism, c) surface plot of Raman intensity for irradiated A-PLA, d) Raman intensity at 2945 $1/\text{cm}$, e) Raman intensity as a function of Raman shift and the spatial coordinate, f) Raman intensity at 2945 $1/\text{cm}$, g) Raman intensity at 1770 $1/\text{cm}$, and h) the ratio of Raman intensities as a function of UV-C dose.

sources [25,35], we would like to point out that the mechanism of photodegradation is of considerable complexity if oxygen is involved. Several authors have proposed mechanisms that lead to an increasing number of oxygen-containing functional groups [37,38]. Therefore, our quantitative analysis of degradation will also include the monitoring of the amplitude of peaks belonging to oxygen-containing groups, such as the carbonyl group.

Since Raman spectrophotometry can provide spatial resolution, different regions of the same sample can be analysed separately. We used this feature to gain information about the effect of irradiation in regions located underneath the surface. In the case of the amorphous samples, we observed a very clear tendency. At the beginning of the experiment ($d = 0 \text{ kJ/m}^2$), the number of functional groups did not depend on the spatial coordinate. However, after irradiation started, the formation of new functional groups led to increased Raman intensities. Furthermore, the increase in the number of functional groups shows spatial coordinate dependence: the closer the investigated point is to the surface, the larger the number of new functional groups is (Fig. 4/d). Although photons can reach the innermost layer of the sample, the effect of degradation is especially pronounced in the region located $\sim 50 \mu\text{m}$ beneath the surface; see Fig. 4/c. This value aligns well with the results of earlier studies that targeted the analysis of penetration depth of UV-C radiation [39,40].

Although Fig. 4/d shows the spatial coordinate dependence of the peak with the largest amplitude (located at 2945 1/cm , see Fig. 4/a), the tendency outlined above is not limited to one single peak. If we select any peak affected by degradation and plot the consecutive spectra belonging to different spatial coordinates, the amplitudes will outline a tendency with a global minimum located inside the film (see Fig. 4/e). This tendency highlights again that new functional groups are formed with a higher probability near the surface. While the rate of degradation depends on the spatial coordinate, it appears to be independent of the orientation of the film. The amplitude increases at the same rate on both sides of the sample, even though only one of them was facing the light source (see Fig. 4/e).

Orientation-independence is caused by the characteristics of photon scattering. In air, the scattering of UV photons obeys the Rayleigh equation, which determines that the intensity of scattered photons is proportional to their frequency raised to the power of four ($I_s \sim f^4$). In practice, this proportionality means that high-frequency photons, such as the UV-C photons used in our experiments, are very prone to scattering and are present in regions of the chamber not directly irradiated by the UV lamp. High-intensity scattering also means that UV photons will enter the gap between the sample and the floor of the degradation chamber and will have the same probability density in this gap as in the remaining space of the chamber. Therefore, the statistical probability of a UV photon crossing the polymer-air interface will not depend on whether the interface is pointing upwards or downwards.

Regarding Fig. 4/e, we also would like to point out that the majority of the peaks are affected by the irradiation, i.e., most of them show a global minimum along the spatial coordinate. To graphically demonstrate this, we plotted the entire measured wavenumber range against the spatial coordinate. The resulting plot has two independent variables (Raman shift and spatial coordinate) and one dependent variable (Raman intensity). The surface function obtained in this way is presented in Fig. 4/c. We have also prepared a video file that demonstrates an animated version of the surface function and it is available as a Supporting Information file S1.

The Raman spectroscopy-based quantitative analysis of photodegradation also enables the characterisation of reaction kinetics. We plotted the Raman intensities of the same spatial coordinates against the UV-C dose as can be seen in Fig. 4/f. The resulting diagram reveals strong positive correlation between the UV-C dose and the amplitude. In this context, positive correlation means that the ongoing degradation permanently increases the total number of new functional groups that resonate at the investigated wavenumber. A positive correlation can also

be observed at wavenumbers that belong to functional groups containing oxygen (Fig. 4/g).

A direct comparison of Figs. 4/f and 4/g enables the estimation of the reaction rate constants. Even though the amplitude of the peak that belongs to the aliphatic end groups (Fig. 4/f) and the $-\text{COO}-$ (such as peroxide) groups (Fig. 4/g) are both increased by the degradation, their rate is different. The ratio of Raman intensities at 2945 1/cm (aliphatic end group) and 874 1/cm ($-\text{COO}-$) appears to be increasing with increasing dose (Fig. 4/h). In practice, this tendency means that the higher the UV-C dose, the higher the probability of the formation of a new functional group that contains oxygen. The dose-dependent rate of the formation of $-\text{COO}-$ groups is due to the differing activation energy barriers of the oxidation of the macromolecular chain at different locations. At the end of the chain, the oxidation of the macromolecule is hindered by a comparatively smaller activation energy barrier. Therefore, the statistical probability of the oxidation of the end of the chain is larger than the probability of the oxidation of a carbon atom located in the middle of the chain. This disparity also means that the more chain ends are in the macromolecular matrix, the higher the statistical probability of oxidation, i.e., the formation of a functional group that contains oxygen. Since degradation leads to the fragmentation of the macromolecules (see Fig. 4/b), the number of chain ends is continuously increased with increasing dose. Therefore, the probability of the formation of oxygen-containing groups is also being increased, as proven by Fig. 4/h.

3.1.3. Changes in thermal properties (MDSC results)

Fig. 5 shows the MDSC thermograms of the neat and the irradiated A-PLA and SC-PLA films within the $20 \text{ }^\circ\text{C}$ – $180 \text{ }^\circ\text{C}$ range. The total heat flow signals of the 1st heat cycle were separated into their reversing and non-reversing components. An average crystallinity of 43 % (calculated with ΔH_{m2}^0) was achieved by heat treatment ($100 \text{ }^\circ\text{C}$ for 2 h), with the appearance of crystal polymorphism with α' and α crystals (Fig. 6/a). It is established in the literature that α' and α crystals co-develop under these post-crystallisation conditions [41]. The crystal polymorphs are very similar, orthorhombic, mainly differ in their unit cell geometry, and α' polymorphs have lower density and contain more defects. Therefore, their thermal stability, melting temperature, and melting enthalpy tend to be lower [42,43].

Initially, the melt temperatures are $150.8 \text{ }^\circ\text{C}$ and $169.2 \text{ }^\circ\text{C}$ for α' and α polymorphs, respectively (Fig. 6/d). With increasing UV-C dose, T_m decreased for α crystals but increased for α' crystals. At $d = 2214 \text{ kJ/m}^2$,

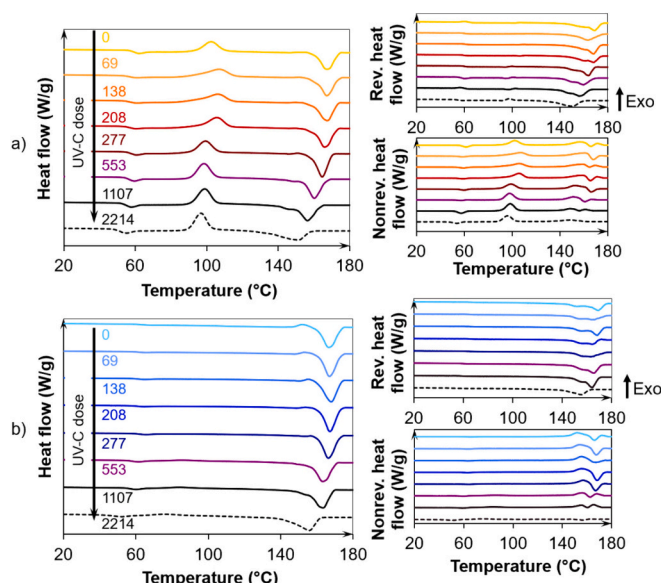


Fig. 5. Heat flow of the a) A-PLA and b) SC-PLA samples.

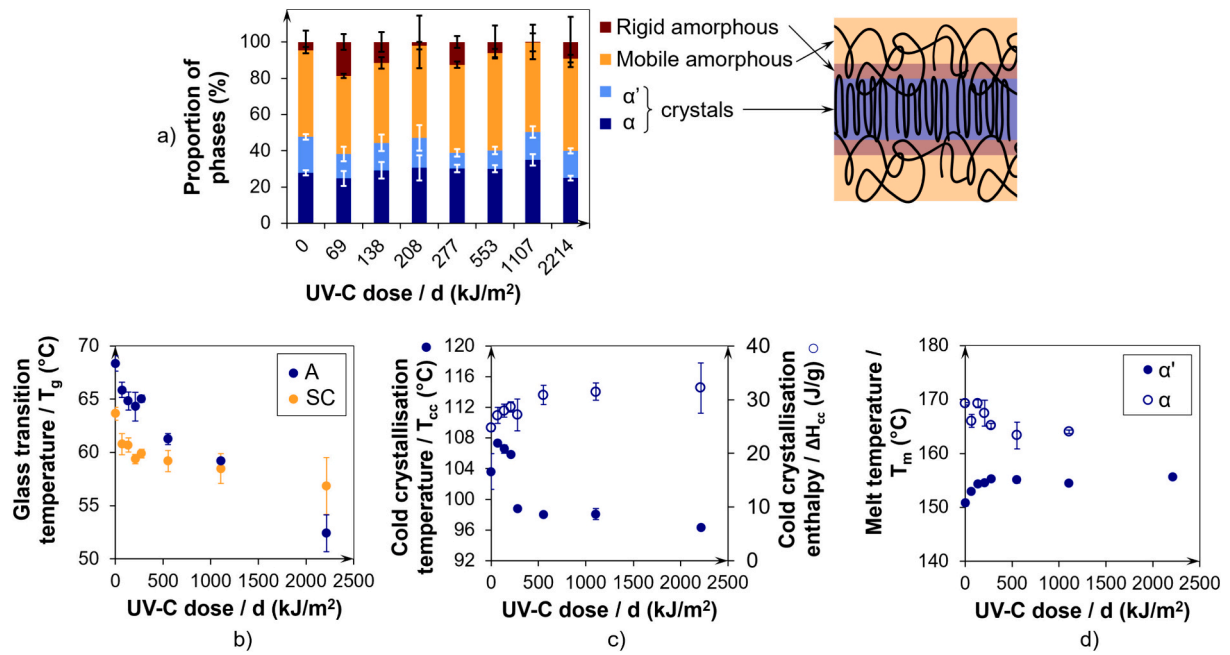


Fig. 6. Changes in the thermal properties due to UV-C irradiation: a) proportion of phases in the SC-PLA, b) glass transition temperature (T_g), c) cold crystallisation temperature (T_{cc}) and enthalpy, d) melt temperature (T_m) (Crystallinity was calculated with ΔH_{m2}^0).

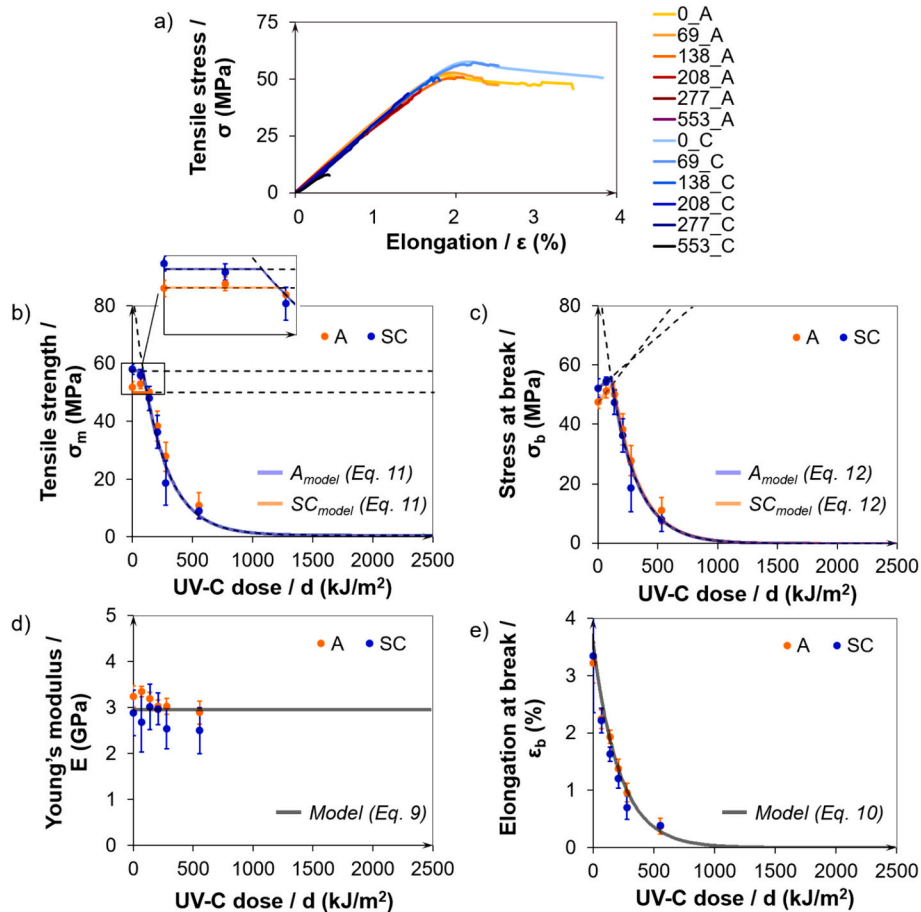


Fig. 7. The deterioration of the tensile properties due to UV-C irradiation: a) mean tensile curves, b) tensile strength, c) stress at break, d) Young's modulus e) elongation at break as a function of UV-C dose.

the two peaks are merged and only a single peak can be seen at around 160 °C. Fig. 6/a shows that the proportion of crystals was unaffected by irradiation, and the ratio of rigid amorphous and mobile amorphous regions also remained unchanged. In contrast, Nugroho et al. [44] found that the radiation-induced degradation of PLA films started in the amorphous regions at lower doses and continued in the crystalline regions under gamma irradiation. Our results suggest that UV-C radiation-induced degradation occurs homogeneously regardless of material structure.

Glass transition temperatures were determined from the reversing heat flow signals of the 1st heating cycles (Fig. 6/b). Post-crystallisation increased the T_g of the neat PLA from 63.6 °C to 68.4 °C. The T_g of the A-PLA and the SC-PLA decreased linearly with increasing UV-C dose, but in the case of the SC-PLA, the rate of the decrease was greater. At an irradiance of 1107 kJ/m², the T_g of the A-PLA and the SC-PLA samples was the same. The reduction in T_g is due to chain scission caused by the UV-C radiation, as segmental movements of shorter molecule chains is initiated at lower temperatures. Fig. 6/c shows the cold crystallisation temperature (T_{cc}) and cold crystallisation enthalpy (ΔH_{cc}) calculated from the non-reversing heat flow signal of the 1st heating ramp, in the case of the A-PLA. Crystals could not form during the production of the films due to rapid cooling, but cold crystallisation occurred in the DSC pan due to heating. T_{cc} follows a decreasing trend with increasing UV-C dose, while the ΔH_{cc} shows a saturation curve. Pan et al. [45] also reported a similar phenomenon that T_{cc} shifts to higher temperatures with increasing molar mass.

3.2. Changes in mechanical behaviour due to UV-C irradiance

3.2.1. The deterioration of tensile properties (tensile test results)

The changes in the tensile properties due to UV-C irradiation are shown in Fig. 7. Fig. 7/a shows the average stress-strain curves for A- and SC-PLA specimens at different UV-C doses.

Post-crystallisation increased the tensile strength and the stress at break of the reference specimens by 9 % and 10 %, respectively (Table 1). However, there was no difference in strength and stress between A- and SC-PLA specimens after irradiation (Fig. 7/b, c). This can be because strength is a minimum property, therefore crack propagation most likely will start and run through in the weakest part (amorphous regions). The tensile test results show that post-crystallisation did not change the Young's modulus (Fig. 7/d). Similar results were obtained by Tsuji et al. [46]. Zhou et al. [47] found that the Young's modulus of PLA films depends on the crystallinity and the proportion of α and α' crystals. However, at room temperature, both the amorphous and the crystalline regions are in a glassy state, therefore their resistance to deformation is high.

The temperature-dependent viscoelastic properties are presented in Section 3.2.2, where the effects of crystallinity are more pronounced. The curves of the degraded samples have the same shape as the curves of the undegraded PLA, but degraded specimens tend to break at lower strains. The dependence of tensile properties on the UV-C dose (d) can be described with suitable functions. The glassy modulus is not influenced

Table 1

Parameters describing the UV-C dose dependence of tensile properties and the RMSE values.

Tensile property	Fitted parameters	Values	RMSE
E	A_E (GPa)	2.94	0.43
ϵ_b	A_ϵ (MPa)	3.23	0.36
	B_ϵ (MPa)	$-4.58 \cdot 10^{-3}$	–
σ_m	A	A_σ (MPa)	52.3
	SC	A_σ (MPa)	57.0
σ_b	A	B_σ (MPa·(m ² /kJ))	0.0525
		C_σ (MPa)	47.6
	SC	B_σ (MPa·(m ² /kJ))	0.0350
		C_σ (MPa)	52.2

by molar mass [48] and do not vary as a function of crystallinity at room temperature. Therefore, we used a fitted constant (A_E) to describe $E(d)$, (Eq. 9):

$$E(d) = A_E, \quad (9)$$

We found that an exponential function can describe the dose dependence of ϵ_b (Eq. 10). As there was no significant difference in ϵ_b between A- and SC-PLA specimens (Fig. 7/e), neither qualitatively nor quantitatively, one function was used to describe both cases.

$$\epsilon_b(d) = A_\epsilon \cdot e^{B_\epsilon \cdot d} \quad (10)$$

where A_ϵ and B_ϵ are fitted constants.

σ_m is constant up to the critical dose (d_{crit}) [49,50], therefore we used Eq. 11 to model its dependence on the UV-C dose. $\sigma_b(d)$ was approximated with Eq. 12. Consequently, we define d_{crit} as a limit above which σ_m is constant ($d_{crit} \approx 131$ kJ/m²). At $d = 1000$ kJ/m², $\epsilon_b(d)$, $\sigma_b(d)$ and $\sigma_m(d)$ are all close to zero, which is consistent with the measured results.

$$\sigma_m(d) = \begin{cases} A_\sigma, & \text{if } d < d_{crit} \\ A_E \cdot (A_\epsilon \cdot e^{B_\epsilon \cdot d}), & \text{if } d > d_{crit} \end{cases} \quad (11)$$

$$\sigma_b(d) = \begin{cases} B_\sigma \cdot d + C_\sigma, & \text{if } d < d_{crit} \\ A_E \cdot (A_\epsilon \cdot e^{B_\epsilon \cdot d}), & \text{if } d > d_{crit} \end{cases} \quad (12)$$

where A_σ , B_σ and C_σ are fitted constants. The values of the fitted parameters and the goodness of the fit are shown in Table 1. Overall, the models describe tensile strength, stress at break and elongation at break well. The measured Young's moduli showed a larger standard deviation, therefore the fit was less accurate.

If $d > d_{crit}$, the stress-strain relationship is quasi-linear and $\sigma(d) = \sigma_b(d) = \sigma_m(d)$, the $0 < \epsilon < \epsilon_b(d = d_{crit})$ region can be approximated with Hooke's law, with Eqs. 9–10. Eqs. 9–12 show that to model the total tensile curve, we only need to consider the dose-dependent ϵ_b , the other parameters are given as a function of it. Therefore, the tensile curve ($\sigma(\epsilon)$) can be written by Eq. 13 as the pointwise minimum of Eq. 14–16 functions.

$$\sigma(\epsilon) = \min_{0 \leq \epsilon \leq \epsilon_b} (\sigma_1(\epsilon), \sigma_2(\epsilon), \sigma_3(\epsilon)), \quad (13)$$

where:

$$\sigma_1(\epsilon) = A_E \cdot \epsilon \quad (14)$$

$$\sigma_2(\epsilon) = A_\sigma \quad (15)$$

$$\sigma_3(\epsilon) = B_\sigma \cdot \left(\frac{\ln\left(\frac{\epsilon}{A_\epsilon}\right)}{B_\epsilon} \right) + C_\sigma \quad (16)$$

From Eq. 13, we obtain the model that describes the total tensile behaviour of the undegraded PLA. In the case of A-PLA, the model consists of three parts. In the case of SC-PLA, the model has two parts. Eq. 10 gives the dose dependence of the elongation at break. Therefore, with the combination of Eq. 13 and Eq. 10, the tensile curves of the degraded PLAs can be obtained (Fig. 8). Figs. 8/a and b illustrate the application of the proposed model for an A-PLA irradiated with a dose of $d = 69$ kJ/m² and an SC-PLA irradiated with $d = 277$ kJ/m², respectively. In both cases the discrete measurement curves and the model curves show good agreement.

The proposed models can be used to estimate the tensile properties of amorphous and semi-crystalline PLA films as a function of UV-C dose. Therefore, the mechanical properties of PLA films can be tailored with UV-C light. Moreover, UV-C irradiation is often used for sterilisation [51], during which the properties of the material deteriorate. With a clear understanding of how UV-C doses affect the mechanical properties of PLA films, sterilisation processes can be optimised to maintain the

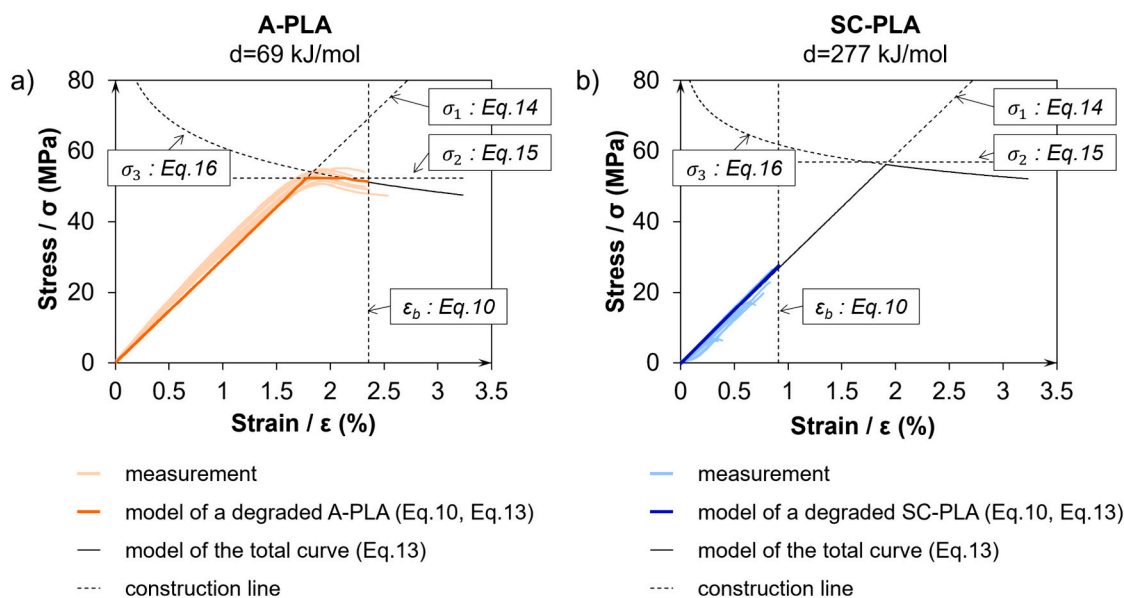


Fig. 8. Estimation of the tensile curve of the degraded PLAs: A-PLA irradiated with $d = 69$ kJ/mol (a) and SC-PLA irradiated with $d = 277$ kJ/mol (b).

integrity and safety of PLA-based products. However, the model specifically describes amorphous and semi-crystalline PLA films. This limits its applicability to other types of polymers. As different polymers might react differently to UV-C irradiation, separate models might be needed for generalised predictions.

3.2.2. Changes in the temperature-dependent viscoelastic properties (dynamic test results)

The dynamic mechanical properties of the films are shown in Fig. 9. The temperature-dependent storage modulus $E'(T)$ shows the resistance of the material to uniaxial tensile deformation as a function of temperature. Fig. 9/a shows that there is no significant difference between the $E'(T)$ values in the glassy state, regardless of crystallinity and the UV-C dose. The average modulus at 40 °C was 2400 ± 260 MPa. This is in good agreement with the Young's modulus results obtained from the tensile tests.

For SC-PLA specimens, a gradual glass transition can be observed, resulting in an order of magnitude decrease in modulus. For the amorphous specimens, the decrease is 3 orders of magnitude. However, between 80 and 100 °C the modulus starts to increase due to recrystallisation and increases by an order of magnitude to 106 ± 15 MPa. In the case of the SC-PLA specimens, $E'(T)$ is also independent of the UV-C dose in the rubbery plateau region with an average value of 161 ± 30 MPa at 140 °C.

We normalised each data series with their own maximum value (Fig. 9/b). In the case of SC-PLA, glass transition shifted towards lower temperatures with increasing UV-C dose. This was also observed in the MDSC results. Meanwhile, the A-PLA samples showed a stochastic transition process between 50 °C and 70 °C. It can be concluded that for SC-PLA, increasing the UV-C dose only influences $E'(T)$ at the glass transition (between 55 and 90 °C), resulting in shift of the inflexion point (which can be associated with T_g) towards lower temperatures.

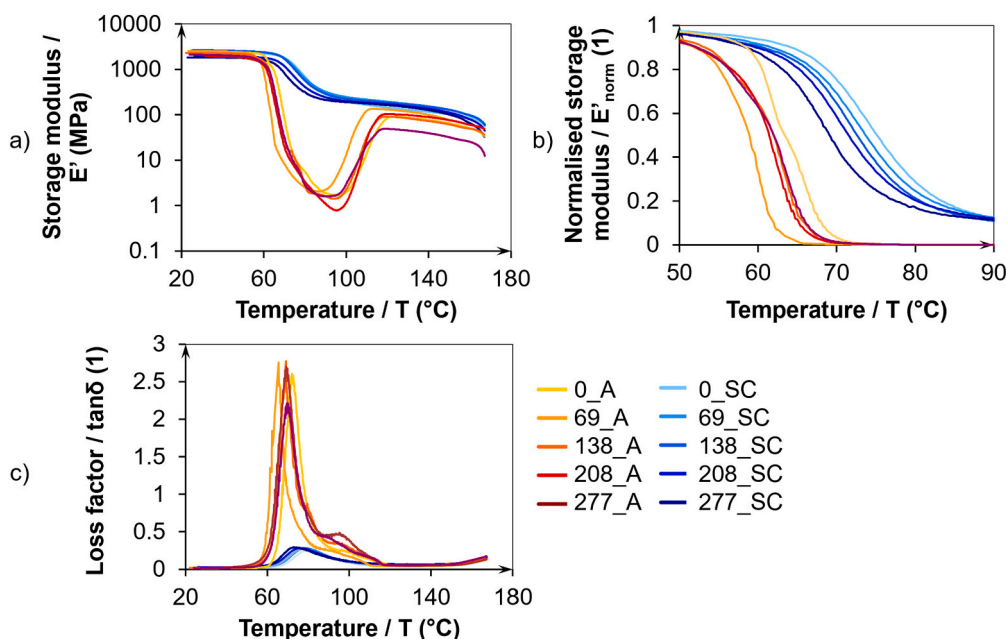


Fig. 9. Changes in temperature-dependent dynamic mechanical properties due to UV-C irradiation: a) storage modulus, b) normalised storage modulus, c) loss factor.

Molecular changes due to heat can be studied with the loss factor ($\tan\delta$) curves (Fig. 9/c). The peak of the curves can be related to glass transition, where T_g is often determined from the maximum peak. The area under the curve is related to chain segment mobility [52]. In the case of the SC-PLA, the area under the curve is considerably smaller than in the case of A-PLA, because the segmental motion of the chains is limited by the crystalline parts. Similar to the $E'(T)$ curves, the SC-PLA also showed the peak shifting towards lower temperatures with increasing UV-C dose, while the A-PLA showed more of a stochastic transition. These temperature sweeps can also be used to optimise the further processing of irradiated films, e.g. to determine the processing window for thermoforming [53,54].

3.2.3. Changes in viscosity due to UV-C irradiation

We measured complex viscosity ($\eta^*(\omega)$) with an oscillatory shear rheometer to investigate the flow properties of the PLA melts. The curves were converted to shear flow viscosity curves ($\eta(\dot{\gamma})$) assuming the Cox-Merz rule applies [55]. Fig. 10/a and 10/c shows that viscosity decreases with increasing UV-C dose. This is expected, as the shorter the chains, the lower the resistance to shear. We observed a 4 % difference in the zero shear viscosities between the neat A-PLA and the SC-PLA samples (Table 3). This is in good agreement with the GPC results, where the molar mass of SC-PLA was decreased by 5 %. The decrease can be due to the post-crystallisation treatment.

As a function of irradiation dose, the viscosity curves varied trendwise from 0 to 208 kJ/m² and can therefore be described by models. First, we fitted the Cross-model [56] (Eq. 17) to the viscosity curves of the neat PLA samples ($d = 0$ kJ/m²).

$$\eta(\dot{\gamma}d) = \frac{\eta_0}{1 + \left(\frac{\eta_0 \dot{\gamma}}{A_\eta}\right)^{1-B_\eta}} \quad (17)$$

where η_0 , A_η and B_η are fitted parameters. η_0 is the zero-shear viscosity, A_η is the critical shear stress at the transition between the Newtonian and power law region and B_η is the power law index.

The same model was then fitted with fixed parameters (A_η, B_η) for all cases between $d = 0$ and $d = 208$ kJ/m². In our previous study [25], we showed that there is a correlation between UV-C dose and viscosity. Here, we establish a relationship using a modified Cross-WLF model

(where we consider the irradiation dose instead of the temperature effect) to describe the effect of UV-C dose on viscosity (Eq.18–19).

$$\eta(\dot{\gamma}d) = \frac{\eta_0(d)}{1 + \left(\frac{\eta_0(d)\dot{\gamma}}{A_\eta}\right)^{1-B_\eta}} \quad (18)$$

$$\eta_0(d) = C_\eta e^{\left[-\frac{D_\eta d}{E_\eta + d}\right]} \quad (19)$$

where C_η , D_η and E_η are fitted constants. The parameter C_η is the zero shear viscosity of the neat PLA ($\eta_0(d = 0)$), and the parameters D_η and E_η are the WLF constants. Eq. (17) was fitted to zero shear viscosities (Fig. 10/b and 10/d). Table 2 shows the fitted constants and the RMSE values.

As a result, we obtained a model (Eqs. 18–19) that can estimate the viscosity curve of the polymer as a function of UV-C dose. The goodness of the model was rated in each case by the normalised relative mean squared error (NRMSE) (Eq. 20). The initial stage of the measurements is uncertain, therefore the NRMSE is calculated for measurement points $\dot{\gamma} > 1$ 1/s.

$$NRMSE = \frac{\sqrt{\sum_{i=1}^n \frac{(\eta_{i,meas} - \eta_{i,model})^2}{n}}}{\eta_0} \cdot 100 \quad (\%) \quad (20)$$

The results are shown in Table 3. Up to 55 % ($d = 208$ kJ/m²)

Table 2
Parameters of the Cross-WLF model.

Fitted parameters	Values	RMSE	
A	A_η (Pa)	$2.29 \cdot 10^5$	-
	B_η (1)	0.19	-
	C_η (Pa·s)	3940	26.16
	D_η (1)	5.3	-
	E_η (kJ/m ²)	163	-
SC	C_η (Pa·s)	3783	16.85
	D_η (1)	6.5	-
	E_η (kJ/m ²)	294	-

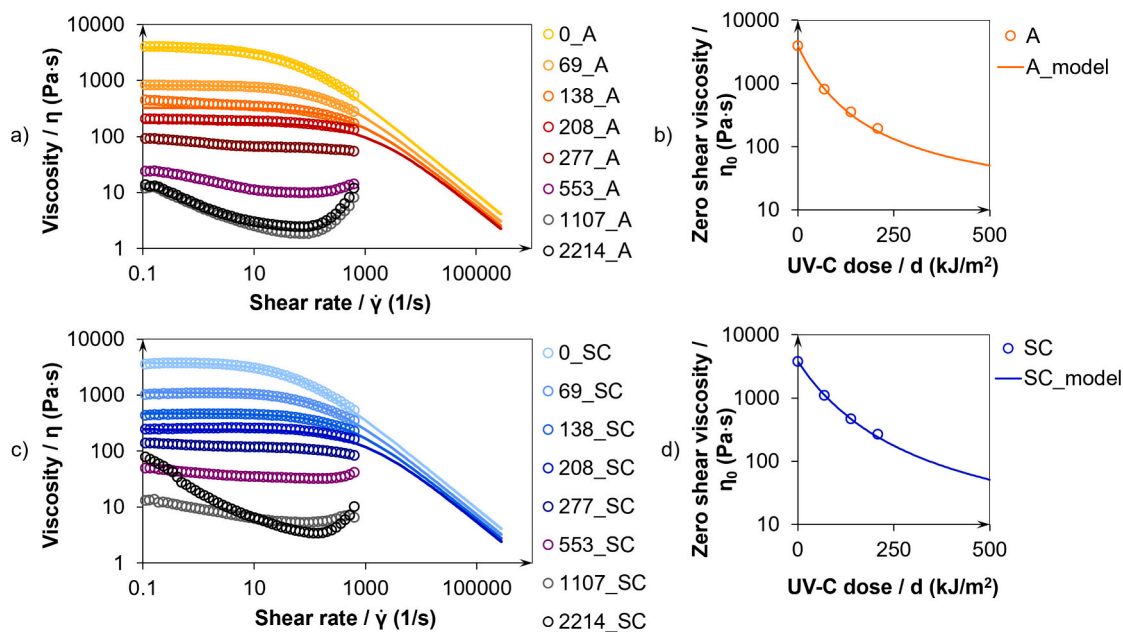


Fig. 10. Changes in viscosity due to UV-C irradiation: viscosity as a function of shear rate for the a) A-PLA and b) SC-PLA. Zero shear viscosity as a function of UV-C dose for the c) A-PLA and the d) SC-PLA. Continuous lines denote the modelled results.

Table 3

Zero-shear viscosities (η_0) and the normalised root mean squared errors (NRMSE) obtained from the Cross-WLF model fit.

d (kJ/m ²)	A		SC	
	η_0 (Pa·s)	NRMSE (%)	η_0 (Pa·s)	NRMSE (%)
0	3940	3.2	3783	0.9
69	821	1.3	1115	1.2
138	325	3.1	468	1.6
208	175	3.3	243	2.9

reduced molar mass the *NRMSE* is below 3.4 %. Therefore, the proposed model can accurately estimate the shear rate-dependent viscosity of UV-C-degraded polymer up to a 55 % reduction of molar mass. It covers the range of shear rates typical for compression moulding, thermoforming, and extrusion (1–10,000 1/s) and is, therefore, suitable for optimising the processing parameters. These findings and the model can be used to develop strategies for recycling and reuse of UV-C irradiated PLA films, contributing to a more sustainable circular economy.

A limitation of the model is that we assume uniform UV-C degradation across the surface of the films, which may not be the case in practical applications. Inhomogeneous degradation can occur due to variations in UV-C exposure or composition, leading to non-uniform changes in viscosity. This discrepancy can result in inaccurate predictions of viscosity, affecting the optimisation of processing parameters and the quality of the final product.

4. Conclusion

In this study, we investigate the effects of UV-C irradiation on amorphous (A-PLA) and semi-crystalline polylactic acid (SC-PLA) films. A- and SC-PLA samples were irradiated with different UV-C doses up to 2214 kJ/m². An average crystallinity of 43 % was achieved by heat treatment. MDSC showed that crystallinity, crystal polymorphs and the ratio of rigid amorphous and mobile amorphous phases were unaffected by irradiation. GPC showed that the degradation mechanism was non-catalytic random scission and the initial molar mass was reduced by >90 % at a dose of 2214 kJ/m² for both A- and SC-PLA samples. The rate of degradation was unaffected by the presence of crystalline parts up to a dose level of 553 kJ/m², but then slightly slowed down for SC-PLA. The Raman spectra obtained from the cross-sections of the films showed that the probability of the formation of oxygen-containing groups increases with increasing UV-C dose. We proposed models to predict the mechanical and rheological properties as a function of UV-C dose. We approximated the UV-C dependence of tensile properties (tensile strength, tensile stress, Young's modulus and elongation at break) with suitable functions and proposed a method to describe the overall tensile curve. We also proposed a modified Cross-WLF model which can accurately describe the effect of UV-C irradiation on viscosity up to 55 % molar mass reduction (highest *NRMSE* was 3.3 %). Our results provide a comprehensive picture of the effects of UV-C radiation on the molecular structure and thermal, rheological and mechanical properties of amorphous and crystalline PLA. By using the proposed models to predict mechanical and rheological properties as a function of UV-C dose, producers can design PLA products optimised for both durability and recyclability. This knowledge can facilitate the creation of more effective recycling processes by accurately estimating the degradation limits and reusability potential of PLA products, contributing to a more sustainable circular economy.

Supplementary data to this article can be found online at <https://doi.org/10.1016/j.ijbiomac.2024.134247>.

CRedit authorship contribution statement

Ábris Dávid Virág: Writing – original draft, Validation, Methodology, Investigation, Conceptualization. **Csenge Tóth:** Writing – original

draft, Visualization, Investigation, Conceptualization. **Péter Polyák:** Writing – original draft, Visualization, Investigation. **Marta Musiol:** Writing – original draft, Investigation. **Kolos Molnár:** Writing – review & editing, Supervision, Funding acquisition.

Declaration of competing interest

The authors declare that they have no known competing financial interests or personal relationships that could have appeared to influence the work reported in this paper.

Data availability

Data will be made available on request.

Acknowledgements

Project no. TKP-9-8/PALY-2021 has been implemented with the support provided by the Ministry of Culture and Innovation of Hungary from the National Research, Development and Innovation Fund, financed under the TKP2021-EGA funding scheme. The research reported in this paper was supported by the H2020-MSCA RISE No. 872152 - GREEN-MAP project of the European Union. Ábris Dávid Virág is thankful for the support of the ÚNKP-23-3-II-BME-178 New National Excellence Program of the Ministry for Culture and Innovation from the source of the National Research, Development and Innovation Fund. The research reported in this paper was supported by the National Research, Development and Innovation Office (FK 138501). The authors are grateful to Benjámín Sándor Gyarmati for access to the rotational rheometer of the Department of Physical Chemistry and Materials Science at the Budapest University of Technology and Economics.

References

- [1] N.P. Tiptis, D.J. Burgess, Sterilization of implantable polymer-based medical devices: a review, *Int. J. Pharm.* 544 (2018) 455–460, <https://doi.org/10.1016/j.ijpharm.2017.12.003>.
- [2] W.J. Rogers, Sterilisation techniques for polymers, *Sterilisation of Biomaterials and Medical Devices* (2012) 151–211, <https://doi.org/10.1533/9780857096265.151>.
- [3] P. Toh-Ae, R. Lee-Nip, Y. Nakaramontri, Releasing of zinc ions from modified zinc oxide surfaces for improvement chemical crosslinks and antibacterial properties of acrylonitrile butadiene rubber films, *Express Polym Lett* 17 (2023) 944–963, <https://doi.org/10.3144/expresspolymlett.2023.70>.
- [4] E. Abbate, D. Rovelli, M. Andreotti, C. Brondi, A. Ballarino, Plastic packaging substitution in industry: variability of LCA due to manufacturing countries, *Procedia CIRP* 105 (2022) 392–397, <https://doi.org/10.1016/j.procir.2022.02.065>.
- [5] N. Lukács, K.E. Decsov, B. Molnár, F. Ronkay, K.B. Bocz, Increased processing temperature assisted reactive toughening of poly(lactic acid), *Express Polym Lett* 17 (2023) 169–180, <https://doi.org/10.3144/expresspolymlett.2023.12>.
- [6] H. Pouriman, K. Graham, K. Jayaraman, Monolayer films from poly(lactic acid) PLA/poly(3-hydroxybutyrate-co-hydroxyvalerate) PHBV blends for food packaging applications, *Express Polym Lett* 17 (2023) 1007–1018, <https://doi.org/10.3144/expresspolymlett.2023.75>.
- [7] S. Liu, S. Qin, M. He, D. Zhou, Q. Qin, H. Wang, Current applications of poly(lactic acid) composites in tissue engineering and drug delivery, *Compos B Eng* 199 (2020) 108238, <https://doi.org/10.1016/j.compositesb.2020.108238>.
- [8] N. Ployetchara, P. Suppakul, D. Atong, C. Pechyen, Blend of polypropylene/poly(lactic acid) for medical packaging application: physicochemical, thermal, mechanical, and barrier properties, *Energy Procedia* 56 (2014) 201–210, <https://doi.org/10.1016/j.egypro.2014.07.150>.
- [9] M. Arastouei, M. Khodaei, S.M. Atyabi, M. Jafari Nodoushan, The in-vitro biological properties of 3D printed poly lactic acid/akermanite composite porous scaffold for bone tissue engineering, *Mater Today Commun* 27 (2021) 102176, <https://doi.org/10.1016/j.mtcomm.2021.102176>.
- [10] Z.A. Alhulaybi, Fabrication and characterization of poly(lactic acid)-based biopolymer for surgical sutures, *ChemEngineering* 7 (2023), <https://doi.org/10.3390/chemengineering7050098>.
- [11] N.E. Duygulu, F. Gifci, C.B. Ustundag, Electrospun drug blended poly(lactic acid) (PLA) nanofibers and their antimicrobial activities, *J. Polym. Res.* 27 (2020) 232, <https://doi.org/10.1007/s10965-020-02215-0>.
- [12] S. Pérez Davila, L. González Rodríguez, S. Chiussi, J. Serra, P. González, How to sterilize polylactic acid based medical devices? *Polymers (Basel)* 13 (2021) <https://doi.org/10.3390/polym13132115>.
- [13] N. Krug, J.-C. Zarges, H.-P. Heim, Influence of ethylene oxide and gamma irradiation sterilization processes on the degradation behaviour of poly(lactic acid)

- (PLA) in the course of artificially accelerated aging, *Polym. Test.* 132 (2024) 108362, <https://doi.org/10.1016/J.POLYMERTESTING.2024.108362>.
- [14] N.M. Ivanova, E.O. Filipova, D.A. Karpov, V.F. Pichugin, Poly(lactic acid) thin films properties after steam sterilization, *Inorg. Mater. Appl. Res.* 11 (2020) 377–384, <https://doi.org/10.1134/S2075113320020148>.
- [15] M. Savaris, V. dos Santos, R.N. Brandalise, Influence of different sterilization processes on the properties of commercial poly(lactic acid), *Mater. Sci. Eng. C* 69 (2016) 661–667, <https://doi.org/10.1016/J.MSEC.2016.07.031>.
- [16] I. Garnica-Bohórquez, V.R. Güiza-Argüello, C.I. López-Gualdrón, Effect of sterilization on the dimensional and mechanical behavior of polylactic acid pieces produced by fused deposition modeling, *Polymers (Basel)* 15 (2023), <https://doi.org/10.3390/polym15153317>.
- [17] N. Krug, J.-C. Zarges, H.-P. Heim, Influence of ethylene oxide and gamma irradiation sterilization processes on the properties of poly-L-lactic-acid (PLLA) materials, *Polymers (Basel)* 15 (2023), <https://doi.org/10.3390/polym15163461>.
- [18] Commission regulation 231/2012 laying down specifications for food additives listed in Annexes II and III to Regulation (EC) No 1333/2008 of the European Parliament and of the Council, *Official Journal L83* (2012) 5.
- [19] U.S. Environmental Protection Agency, Final Amendments to Strengthen Air Toxics Standards for Ethylene Oxide Commercial Sterilizers, 2024.
- [20] M. Mansouri, A. Berrayah, C. Beyens, C. Rosenauer, C. Jama, U. Maschke, Effects of electron beam irradiation on thermal and mechanical properties of poly(lactic acid) films, *Polym. Degrad. Stab.* 133 (2016) 293–302, <https://doi.org/10.1016/J.POLYMEDEGRADSTAB.2016.09.005>.
- [21] P. Benyathiar, S.E. Selke, B.R. Harte, D.K. Mishra, The effect of irradiation sterilization on poly(lactic acid) films, *J. Polym. Environ.* 29 (2021) 460–471, <https://doi.org/10.1007/s10924-020-01892-8>.
- [22] M.A. Aboamer, A.S. Alsuayri, A. Alassaf, T.M. Alqahtani, B.A. Alresheedi, G. N. Saijari, E.A. Osman, N.A.R. Mohamed, Hybrid radiant disinfection: exploring UVC and UVB sterilization impact on the mechanical characteristics of PLA materials, *Polymers (Basel)* 15 (2023), <https://doi.org/10.3390/polym15244658>.
- [23] C.G. Amza, A. Zapciu, F. Baciu, M.I. Vasile, D. Popescu, Aging of 3d printed polymers under sterilizing uv-c radiation, *Polymers (Basel)* 13 (2021), <https://doi.org/10.3390/polym13244467>.
- [24] M.H. Brown, T.D. Badzinski, E. Pardoe, M. Ehlebracht, M.A. Maurer-Jones, UV light degradation of polylactic acid kickstarts enzymatic hydrolysis, *ACS Materials* Au (2023), <https://doi.org/10.1021/acsmaterialsau.3c00065>.
- [25] Á.D. Virág, C. Tóth, K. Molnár, Photodegradation of polylactic acid: characterisation of glassy and melt behaviour as a function of molecular weight, *Int. J. Biol. Macromol.* 252 (2023) 126336, <https://doi.org/10.1016/J.IJBIOMAC.2023.126336>.
- [26] T. Standau, C. Zhao, S.M. Castellón, C. Bonten, V. Altstädt, Chemical modification and foam processing of polylactide (PLA), *Polymers (Basel)* 11 (2019), <https://doi.org/10.3390/polym11020306>.
- [27] H.M. Yoo, S.-Y. Jeong, S.-W. Choi, Analysis of the rheological property and crystallization behavior of polylactic acid (Ingeo™ biopolymer 4032D) at different process temperatures 21 (2021) 702–709, <https://doi.org/10.1515/epoly-2021-0071>.
- [28] E. Zuzá, J.M. Ugartemendia, A. Lopez, E. Meaurio, A. Lejardi, J.R. Sarasua, Glass transition behavior and dynamic fragility in polylactides containing mobile and rigid amorphous fractions, *Polymer (Guildf)* 49 (2008) 4427–4432, <https://doi.org/10.1016/J.POLYMER.2008.08.012>.
- [29] S. Gogolewski, P. Mainil-Varlet, Effect of thermal treatment on sterility, molecular and mechanical properties of various polylactides: 2. Poly(l/d-lactide) and poly(l/dl-lactide), *Biomaterials* 18 (1997) 251–255, [https://doi.org/10.1016/S0142-9612\(96\)00132-9](https://doi.org/10.1016/S0142-9612(96)00132-9).
- [30] S. Belbachir, F. Zairi, G. Ayoub, U. Maschke, M. Naït-Abdelaziz, J.M. Gloaguen, M. Benguediab, J.M. Lefebvre, Modelling of photodegradation effect on elastic-viscoplastic behaviour of amorphous polylactic acid films, *J. Mech. Phys. Solids* 58 (2010) 241–255, <https://doi.org/10.1016/j.jmps.2009.10.003>.
- [31] W. Sakai, N. Tsutsumi, Photodegradation and radiation degradation, *Poly(Lactic Acid)* (2022) 439–454, <https://doi.org/10.1002/9781119767480.ch19>.
- [32] A. Gleadall, J. Pan, M.A. Kruff, M. Kellomäki, Degradation mechanisms of bioresorbable polyesters. Part 1. Effects of random scission, end scission and autocatalysis, *Acta Biomater.* 10 (2014) 2223–2232, <https://doi.org/10.1016/j.actbio.2013.12.039>.
- [33] E. Bolskis, E. Adomavičiūtė, E. Griškonis, Formation and investigation of mechanical, thermal, optical and wetting properties of melt-spun multifilament poly(lactic acid) yarns with added rosins, *Polymers (Basel)*. 14 (2022) 379, <https://doi.org/10.3390/polym14030379>.
- [34] M.A. Cuiffo, J. Snyder, A.M. Elliott, N. Romero, S. Kannan, G.P. Halada, Impact of the fused deposition (FDM) printing process on polylactic acid (PLA) chemistry and structure, *Appl. Sci.* 7 (2017) 579, <https://doi.org/10.3390/app7060579>.
- [35] C. Zhang, C. Man, W. Wang, L. Jiang, Y. Dan, Degradation of poly(L-lactide) films under ultraviolet irradiation and water bath, *Polym.-Plast. Technol. Eng.* 50 (2011) 810–817, <https://doi.org/10.1080/03602559.2011.551970>.
- [36] C.M.S. Izumi, M.L.A. Temperini, FT-Raman investigation of biodegradable polymers: poly(3-hydroxybutyrate) and poly(3-hydroxybutyrate-co-3-hydroxyvalerate), *Vib. Spectrosc.* 54 (2010) 127–132, <https://doi.org/10.1016/j.vibspec.2010.07.011>.
- [37] E. Olewnik-Kruszkowska, I. Koter, J. Skopińska-Wisniewska, J. Richert, Degradation of polylactide composites under UV irradiation at 254 nm, *J. Photochem. Photobiol. A Chem.* 311 (2015) 144–153, <https://doi.org/10.1016/j.jphotochem.2015.06.029>.
- [38] M.E. González-López, A.S. Martín del Campo, J.R. Robledo-Ortiz, M. Arellano, A. Pérez-Fonseca, Accelerated weathering of poly(lactic acid) and its biocomposites: a review, *Polym. Degrad. Stab.* 179 (2020), <https://doi.org/10.1016/j.polymdegradstab.2020.109290>.
- [39] A. M.B. B. Lobo, Optical properties of UV-C irradiated polyvinylidene chloride films, *Radiat. Phys. Chem.* 212 (2023) 111182, <https://doi.org/10.1016/j.radphyschem.2023.111182>.
- [40] K. Skowron, J. Bauza-Kaszewska, Z. Dobrzański, Z. Paluszak, K.J. Skowron, UV-C radiation as a factor reducing microbiological contamination of fish meal, *Sci. World J.* 2014 (2014) 1–8, <https://doi.org/10.1155/2014/928094>.
- [41] P. Ma, X. Wang, Y. He, Z. Dong, X. Zhang, X. Chen, T. Liu, Effect of poly(lactic acid) crystallization on its mechanical and heat resistance performances, *Polymer (Guildf)* 212 (2021) 123280, <https://doi.org/10.1016/J.POLYMER.2020.123280>.
- [42] J.P. Kalish, K. Aou, X. Yang, S.L. Hsu, Spectroscopic and thermal analyses of α' and α crystalline forms of poly(L-lactic acid), *Polymer (Guildf)* 52 (2011) 814–821, <https://doi.org/10.1016/J.POLYMER.2010.12.042>.
- [43] K. Jariyavidyanont, A. Janke, Q. Yu, T. Thurn-Albrecht, R. Androsch, Lamellar morphology of disorder α' -crystals of poly(L-lactic acid), *Cryst. Growth Des.* 24 (2024) 1825–1834, <https://doi.org/10.1021/acs.cgd.3c01498>.
- [44] P. Nugroho, H. Mitomo, F. Yoshii, T. Kume, Degradation of poly(L-lactic acid) by γ -irradiation, *Polym. Degrad. Stab.* 72 (2001) 337–343, [https://doi.org/10.1016/S0141-3910\(01\)00030-1](https://doi.org/10.1016/S0141-3910(01)00030-1).
- [45] P. Pan, W. Kai, B. Zhu, T. Dong, Y. Inoue, Polymorphous crystallization and multiple melting behavior of poly(L-lactide): molecular weight dependence, *Macromolecules* 40 (2007) 6898–6905, <https://doi.org/10.1021/ma071258d>.
- [46] H. Tsuji, Y. Echizen, S.K. Saha, Y. Nishimura, Photodegradation of poly(L-lactic acid): effects of photosensitizer, *Macromol. Mater. Eng.* 290 (2005) 1192–1203, <https://doi.org/10.1002/mame.200500278>.
- [47] C. Zhou, H. Guo, J. Li, S. Huang, H. Li, Y. Meng, D. Yu, J. de Claville Christiansen, S. Jiang, Temperature dependence of poly(lactic acid) mechanical properties, *RSC Adv.* 6 (2016) 113762–113772, <https://doi.org/10.1039/C6RA23610C>.
- [48] Z. Bin Ahmad, M.F. Ashby, Failure-mechanism maps for engineering polymers, *J. Mater. Sci.* 23 (1988) 2037–2050, <https://doi.org/10.1007/BF01115766>.
- [49] J. Pabiot, J. Verdu, The change in mechanical behavior of linear polymers during photochemical aging, *Polym. Eng. Sci.* 21 (1981) 32–38, <https://doi.org/10.1002/pen.760210106>.
- [50] B. Fayolle, L. Audouin, J. Verdu, Oxidation induced embrittlement in polypropylene — a tensile testing study, *Polym. Degrad. Stab.* 70 (2000) 333–340, [https://doi.org/10.1016/S0141-3910\(00\)00108-7](https://doi.org/10.1016/S0141-3910(00)00108-7).
- [51] C. Olagüe, O. Mitxelena-Iribarren, J.E. Sierra-García, F. Rodríguez-Merino, S. Maestro, E. Pérez-Lorenzo, F. Guillen-Grima, G. González-Aseguinolaza, S. Arana, C. Smerdou, Rapid SARS-CoV-2 disinfection on distant surfaces with UV-C: the inactivation is affected by the type of material, *J. Photochem Photobiol* 11 (2022) 100138, <https://doi.org/10.1016/J.JPAP.2022.100138>.
- [52] M.S. Lin, S.T. Lee, Mechanical behaviours of fully and semi-interpenetrating polymer networks based on epoxy and acrylics, *Polymer (Guildf)* 38 (1997) 53–58, [https://doi.org/10.1016/S0032-3861\(96\)00484-3](https://doi.org/10.1016/S0032-3861(96)00484-3).
- [53] S. Jodeh, Carrier films behavior during thermoforming process studied using dynamic mechanical thermal analysis (DMTA), *J. Polym. Res.* 18 (2011) 939–944, <https://doi.org/10.1007/s10965-010-9491-4>.
- [54] D. Masato, J. Licata, P. Gao, N. Maynard, J. Slocumb, A. Cavanaugh, M. Sterling, C. Moritz, Thermoformability analysis of TPO sheets blended with postindustrial secondary feedstock, *Polym. Eng. Sci.* 63 (2023) 1932–1942, <https://doi.org/10.1002/pen.26335>.
- [55] W.P. Cox, E.H. Merz, Correlation of dynamic and steady flow viscosities, *J. Polym. Sci.* 28 (1958) 619–622, <https://doi.org/10.1002/pol.1958.1202811812>.
- [56] M.M. Cross, Rheology of non-Newtonian fluids: a new flow equation for pseudoplastic systems, *J. Colloid Sci.* 20 (1965) 417–437, [https://doi.org/10.1016/0095-8522\(65\)90022-X](https://doi.org/10.1016/0095-8522(65)90022-X).